Available online at website: https://journal.bcrec.id/index.php/bcrec

Bulletin of Chemical Reaction Engineering & Catalysis, 20 (2) 2025, 264-279

Original Research Article

S-scheme g-C_3N_4/PVA Heterojunction with Enhanced Photocatalytic Reduction of Aqueous Cr(VI) and Mechanism

Tianhong Guo[1], Yingxing Jiang[3], Yuanyuan Luo[2], Xianhui Liang[3], Xinshan Zhao[2], Jing Li[3,*]

[1]Metrology & Test, Shandong Special Equipment Inspection and Testing Group, 25000, Jinan, Shandong, China
[2]School of Chemistry and Environmental Science, Yili Normal University, 835000, Yining, China
[3]School of Materials and Chemical Engineering, Xuzhou University of Technology, 221018, Xuzhou, China

Received: 9th February 2025; Revised: 25th March 2025; Accepted: 26th March 2025
Available online: 27th March 2025; Published regularly: August 2025

Abstract

Bulk g-C_3N_4 was synthesized using melamine as a precursor through thermal polymerization followed by high-temperature quenching. Subsequently, a g-C_3N_4/PVA heterojunction featuring evenly dispersed PVA on its surface was fabricated via in-situ hydrothermal synthesis. The impact of hydrothermal temperature and PVA concentration on the light absorption, bandgap energy, specific surface area, and charge carrier transport characteristics of g-C_3N_4/PVA were explored. Experimental findings indicate that PVA modification reduces nitrogen-vacancy defects in the g-C_3N_4/PVA heterojunction, thereby enhancing its visible-light photocatalytic activity compared to bulk g-C_3N_4. Specifically, g-C_3N_4/PVA-3 exhibits a 2.93-fold higher reaction rate for Cr(VI) photocatalytic reduction under visible light (0.017 min^{-1}) than bulk g-C_3N_4 (0.0058 min^{-1}), with a TOF of 0.0079 h^{-1}. Electrochemical tests confirm that the enhanced activity arises from improved light-induced charge transfer and separation efficiency. Based on Mott-Schottky analysis and the identification of $\cdot OH$ and $\cdot O_2^-$ as reactive species, a mechanism for Cr(VI) reduction by S-scheme g-C_3N_4/PVA heterojunctions is proposed. This study presents an economically viable and efficient method for developing high-performance conjugated polymer-modified photocatalysts.

Keywords: Graphitic carbon nitride; Polyvinyl alcohol; Photogenerated carriers; S-scheme heterojunction; hexavalent chrome

How to Cite: Guo, T., Jiang, Y., Luo, Y., Liang, X., Zhao, X., Li, J. (2025). S-scheme g-C3N4/PVA Heterojunction with Enhanced Photocatalytic Reduction of Aqueous Cr(VI) and Mechanism. *Bulletin of Chemical Reaction Engineering & Catalysis*, 20 (2), 264-279. (doi: 10.9767/bcrec.20350)

Permalink/DOI: https://doi.org/10.9767/bcrec.20350

***Supporting Information* (SI)**: https://journal.bcrec.id/index.php/bcrec/article/downloadSuppFile/20350/5662

1. Introduction

Chromium (Cr) is a ubiquitous chemical element found in natural ecosystems, primarily existing in trivalent (Cr(III)) and hexavalent (Cr(VI)) forms [1–8]. The hexavalent chromium (Cr(VI)) is notorious for its high toxicity, strong oxidizing properties, mutagenicity, and teratogenicity, which can lead to cell membrane damage, pulmonary congestion, and cancer [2,3]. It is commonly found in industrial wastewater from processes such as leather tanning, pigment manufacturing, and metallurgy [7,8]. The toxicity of Cr(VI) is reported to be approximately 3000 times higher than that of Cr(III) [2], which is an essential trace element for human health.

Aqueous Cr(VI) exhibits excellent solubility, high mobility, and non-biodegradability [2–6]. Therefore, using photocatalytic technology to reduce Cr(VI) to Cr(III) is an essential environmental protection strategy [2,3]. Photocatalytic technology, which harnesses solar energy to reduce Cr(VI) to Cr(III), is advantageous

* Corresponding Author.
Email: lijingxz111@163.com (J. Li)

due to its cost-effectiveness, chemical stability, and high activity. Research indicates that the key factors affecting photocatalytic activity include [2,9−16]: (i) the energy band structure of the photocatalyst, which determines the capacity for light absorption; (ii) the generation, separation, and transportation of photogenerated charge carriers induced by light irradiation of the photocatalyst; (iii) the valence band (VB) potential and conduction band (CB) potentials of the photocatalysts, which determine the active species in the photocatalytic reaction and the redox ability of the photo-induced charge carriers. Therefore, developing high-performance photocatalysts is crucial for advancing the application of photocatalytic technology.

Graphitic carbon nitride (g-C_3N_4) is a two-dimensional organic semiconductor photocatalyst known for its excellent chemical and thermal stability. The raw materials for preparing g-C_3N_4 are abundant, such as melamine and other triazine or heptazine derivatives [10], making it suitable for large-scale industrial applications. Importantly, g-C_3N_4 possesses an appropriate bandgap energy (~2.7 eV) [11], which allows it to be excited and drive photocatalytic reactions under visible light. It exhibits excellent photocatalytic activity due to its moderate valence band and conduction band potentials [12−17]. Consequently, g-C_3N_4 has been widely utilized as a photocatalyst across various domains, including hydrogen production [19], CO_2 conversion [20], nitrogen fixation [21], organic synthesis [22], antibiotic degradation [12], and reduction of heavy metal ions [9]. Unfortunately, the photocatalytic efficiency of g-C_3N_4 produced through thermal polymerization is constrained by the fast recombination of photogenerated electron-hole pairs, a limited specific surface area, and a restricted light absorption spectrum [13,14].

It has been demonstrated [13,18,23,24] that the photocatalytic activity of g-C_3N_4 can be significantly enhanced through various modification strategies such as elemental doping, defect introduction, cocatalyst incorporation, protonation treatment, and heterojunction design [23,24]. However, there are few reports on achieving small-sized g-C_3N_4 via the simple, rapid cooling treatment of bulk g-C_3N_4 synthesized through thermal polymerization. Combining g-C_3N_4 with other semiconductors to construct composite materials represents a straightforward and effective strategy [12−17]. This approach leverages the heterogeneous interfaces within the composites to improve the separation and transfer of photogenerated carriers, reduce recombination, increase the surface area, and expand the light absorption range.

Polyvinyl alcohol (PVA), as an organic polymer with excellent biocompatibility, hydrophilicity, and mechanical stability [25], is widely used in food processing and biomedical fields [25,26]. Recent research has shown that treating PVA at high temperatures can generate a conjugated structure with enhanced visible light absorption and charge transfer efficiency, thereby enhancing the photocatalytic performance of inorganic semiconductors [27–29]. For instance, Wang *et al.* [27] demonstrated that CPVA/MoS_2 exhibited significantly improved photocatalytic activity in chromium (VI) reduction. Gao *et al.* [28] incorporated g-C3N4 into a polyvinyl alcohol (PVA) sponge, effectively removing tetracycline (TC) and Rhodamine B (RhB) from wastewater. Furthermore, Chen [29] employed PVA as a solid proton donor to boost the photocatalytic performance of graphitic carbon nitride in hydrogen peroxide production. However, there is limited research on the photocatalytic reduction of Cr(VI) using PVA-modified g-C_3N_4, and a deeper analysis of the photocatalytic reaction mechanism is needed. This study explores the performance and mechanism of visible light photocatalytic reduction of Cr(VI) by the g-C_3N_4/PVA heterojunction.

Although the application of PVA in enhancing photocatalytic performance has been reported in the literature, few studies have focused on its synergistic effect with thermally quenched g-C_3N_4 for Cr(VI) reduction. Notably, the combination of rapid cooling treatment to mitigate nitrogen vacancies and in-situ PVA loading to form an S-scheme heterojunction represents a novel strategy. This approach optimizes the interface charge transfer and enhances visible-light absorption and surface reactivity. Furthermore, the mechanism of PVA in suppressing carrier recombination and generating reactive species ($\cdot OH/\cdot O_2^-$) remains underexplored. Therefore, this study aims to explore the properties and mechanism of visible light photocatalytic reduction of Cr(VI) by g-C_3N_4/PVA heterojunction. g-C_3N_4 was synthesized through thermal polymerization and rapid cooling treatment, and g-C_3N_4/PVA heterojunction was synthesized by hydrothermal technology. The effects of reaction temperature and PVA load on the photocatalytic performance of the composite were studied. The structure-activity relationship of the g-C3N4/PVA composite was systematically studied by combining the photoelectronic performance test and the active species capture experiment. This study provides a new strategy and theoretical basis for treating wastewater containing heavy metal ions.

2. Materials and Method

2.1 Reagents

The following chemicals were used: Melamine ($C_3H_6N_6$, 99.5%), polyvinyl alcohol (PVA, [-CH_2CHOH-]$_n$, 98.0%), diphenyl carbamide

($C_{13}H_{14}N_4O$), nitric acid (HNO_3, 68.0%), acetone (C_3H_6O, 99.5%), sulfuric acid (H_2SO_4, 98.0%), anhydrous ethanol (C_2H_6O). All reagents were purchased from Sinopharm Chemical Reagent Co. and were used without further purification.

2.2 Synthesis

Bulk g-C_3N_4 synthesis. Initially, 3 g of melamine was ground and transferred to a sealed corundum crucible. The crucible was then heated in a ceramic fiber muffle furnace at a rate of 5 ℃/min to 540 ℃ and held at this temperature for 3 h. Subsequently, the crucible was rapidly removed and quenched in pre-cooled ice water, followed by washing the resulting crude product with deionized water and drying to obtain g-C_3N_4.

Preparation of g-C_3N_4/PVA Composite Material. 0.5 g of self-prepared g-C_3N_4 was dispersed in 40 mL of 0.5 mol/L nitric acid solution and thoroughly mixed. Next, 5 mg of PVA was added, stirring the mixture for 30 min. The resulting solution was transferred to a sealed stainless steel autoclave and heated in a convection oven at 150 ℃ for 10 h. The precipitate was filtered, washed with deionized water, and dried to obtain the g-C_3N_4/PVA-1 composite.

Variations were made in the experimental program. Adjusting the heating temperature to 170℃ and 190℃, g-C_3N_4/PVA-2 and g-C_3N_4/PVA-3 were produced, respectively. Increasing the PVA content to 10 mg and 2.5 mg allowed resulted in the preparation of g-C_3N_4/PVA-4 and g-C_3N_4/PVA-5, respectively.

2.3 Characterizations

The composition of the synthesized materials was characterized using a variety of techniques. X-ray powder diffraction (XRD) was performed using an Ultima IV diffractometer (Rigaku Corporation, Japan), and Fourier-transform infrared spectrometer (FT-IR) was conducted with an ALPHA spectrometer (Bruker, Germany). Morphological features were examined using a scanning electron microscope (SEM, SU8600, Hitachi, Japan). The UV-visible-near-infrared diffuse reflectance spectra of the photocatalysts were recorded using a Lambda750 spectrophotometer (PerkinElmer, USA). Specific surface areas and pore structures were determined by Brunauer-Emmett-Teller (BET) analysis using an ASAP 2460 instrument (Micromeritics, USA). Transient photocurrent response (i-t), electrochemical impedance spectroscopy (EIS), and Mott-Schottky (M-S) measurements were performed using an electrochemical workstation (CHI 660E, Shanghai Chenhua Instruments Co., Ltd., China) with a three-electrode system and Ag/AgCl as the reference electrode. Photoluminescence (PL) spectra were obtained using an F-2700 spectrometer (Hitachi, Japan) with an excitation wavelength of 370 nm.

2.4 Photocatalytic Activity Investigation

The photocatalytic activity of g-C_3N_4/PVA was evaluated under the following conditions: 300 mg of the prepared photocatalyst was added to 300 mL of aqueous solution containing 30 mg/L Cr(VI). Initially, an adsorption-desorption equilibrium test was performed in the dark at ambient temperature. After this, a 250 W Xenon lamp, equipped with a filter to block UV light below 420 nm, was turned on to promote the photocatalytic reduction of Cr(VI). During the experiment, 4 mL of the reaction solution was periodically taken out and filtered through a 0.22 μm cellulose acetate membrane to separate the photocatalyst. The concentration of Cr(VI) was measured using diphenylcarbazide spectrophotometry (λ_{max} = 543 nm). The removal efficiency (R%) of Cr(VI) was calculated using Equation (1), where c_0 and c_t denote the concentration of Cr(VI) at 0 and t min, respectively. All photocatalytic experiments were conducted in triplicate under identical conditions to ensure repeatability.

$$R\% = \frac{(c_0 - c_t)}{c_0} x100\% \quad (1)$$

Based on the initial photocatalytic experiment conducted at 25 ℃ (298 K), additional experiments were performed at 293 K and 303 K to systematically evaluate the influence of temperature on the reduction rate of Cr(VI). Furthermore, the impact of catalyst dosage on the reduction of Cr(VI) was also examined.

3. Results and Discussion

3.1. Composition and Structure Analyses

Figure 1 displays the XRD patterns of the synthesized g-C_3N_4, PVA, and g-C_3N_4/PVA heterojunctions. As illustrated in Figure 1(a), it is evident that the graphitic structure of g-C_3N_4 displays two prominent diffraction peaks at 13.20° and 27.40°, corresponding to the (100) and (002) planes of the conjugated aromatic group of g-C_3N_4 (JCPDS Card No. 87-1526) [30]. These peaks are attributed to the in-plane packing of tri-s-triazine segments and the interlayer stacking of conjugated aromatic structures [18]. The XRD pattern of PVA exhibited a diffraction peak at 19.3°, assigned to the (101) plane of polyvinyl alcohol [31]. The XRD patterns of g-C_3N_4/PVA photocatalysts closely resemble those of g-C_3N_4, with no distinct characteristic peak of PVA observed. The Debye-Scherrer formula (Equation

(2)) was utilized to determine the crystallite size (D) of the synthesized photocatalysts [30]. Based on the diffraction data from the (002) plane, the crystallite sizes of g-C_3N_4, g-C_3N_4/PVA-1, g-C_3N_4/PVA-2, g-C_3N_4/PVA-3, g-C_3N_4/PVA-4 and g-C_3N_4/PVA-5 are 5.34, 5.86, 7.54, 7.83, 7.51, and 8.21, respectively. Notably, with the increase in PVA content, the diffraction peak of g-C_3N_4/PVA at 27.40° shifts significantly to a larger angle (Figure S1, Supporting Information), suggesting that the addition of PVA may reduce the interlayer spacing, which is consistent with the inverse relationship between the diffraction angle and the interlayer spacing (Equation (3)) [33], where D is the crystallite size (nm), k represents the Scherrer constant (0.90), λ is the X-ray wavelength (0.15406 nm), β denotes the full-width at half maxima, θ is the angle of diffraction, d refers to the interplanar spacing, and n is the order of reflection.

$$D = \frac{k \times \lambda}{\beta \cos\theta} \quad (2)$$

$$2d = \frac{n \times \lambda}{\sin\theta} \quad (3)$$

The structural information of the prepared photocatalysts was analyzed using FT-IR spectroscopy. Figure 1(b) provides the FT-IR spectra of g-C_3N_4 and g-C_3N_4/PVA heterojunction in the range of 500 cm^{-1} to 3500 cm^{-1}. The absorption peak around 3200 cm^{-1} observed in all samples is attributed to the O-H stretching vibrations from adsorbed water on the samples. The peak at 806 cm^{-1} is caused by the breathing mode of the tri-s-triazine units in g-C_3N_4 [10,17]. Additionally, the infrared absorption peaks at 1242 cm^{-1}, 1338 cm^{-1}, and 1456 cm^{-1} are indicative of the stretching vibrations of aromatic C-N single bonds. The peak observed at 1635 cm^{-1} is associated with the stretching vibrations of both C=N and C=C bonds [27]. These signals indicate the presence of a conjugated structure in the g-C_3N_4/PVA heterojunction.

Figure 2 presents the SEM images of the synthesized g-C_3N_4 and g-C_3N_4/PVA heterojunctions. Specifically, Figure 2(a) provides the morphology of pure g-C_3N_4, which exhibits a smooth bulk structure on the surface. Figure 2(b) to 2(f) demonstrate the morphology of the g-C_3N_4/PVA composites synthesized under different conditions. These composite materials are similar to g-C_3N_4 in morphology but exhibit a rougher surface, which may be due to the formation of a covering layer by PVA on the surface of g-C_3N_4. TEM images revealed the layered structure of g-C_3N_4/PVA-3 (Figure 2(g)), and the PVA coating did not alter the intrinsic layered morphology of g-C_3N_4 (Figure 2(h)). Furthermore, HR-TEM images confirmed that g-C_3N_4 and PVA exhibited amorphous characteristics, with no distinct interface observed at their junction. Figure 2(i), Figure S2 (Supporting Information), and Table S1 (Supporting Information) present the energy-dispersive X-ray (EDX) spectra and elemental mapping images for g-C_3N_4/PVA-3 and bulk-g-C_3N_4. These analyses confirm that g-C_3N_4/PVA-3 is composed of carbon (C), nitrogen (N), and oxygen (O), with a uniform distribution of these elements across the photocatalyst surface, thereby validating the elemental composition of g-C_3N_4/PVA. The EDX data reveal that the atomic ratio of carbon to nitrogen in bulk-g-C_3N_4 exceeds the stoichiometric ratio of 3:4, suggesting the presence of nitrogen vacancies in the thermally polymerized bulk-g-C_3N_4. Modifying polyvinyl alcohol (PVA) in g-C_3N_4/PVA-3 has been observed to mitigate these nitrogen-vacancy defects to a certain extent. According to the thermogravimetric analysis results presented in Figure S3 (Supporting Information), it is evident that pure g-C_3N_4 demonstrates excellent thermal stability below 600 ℃, with a weight loss of

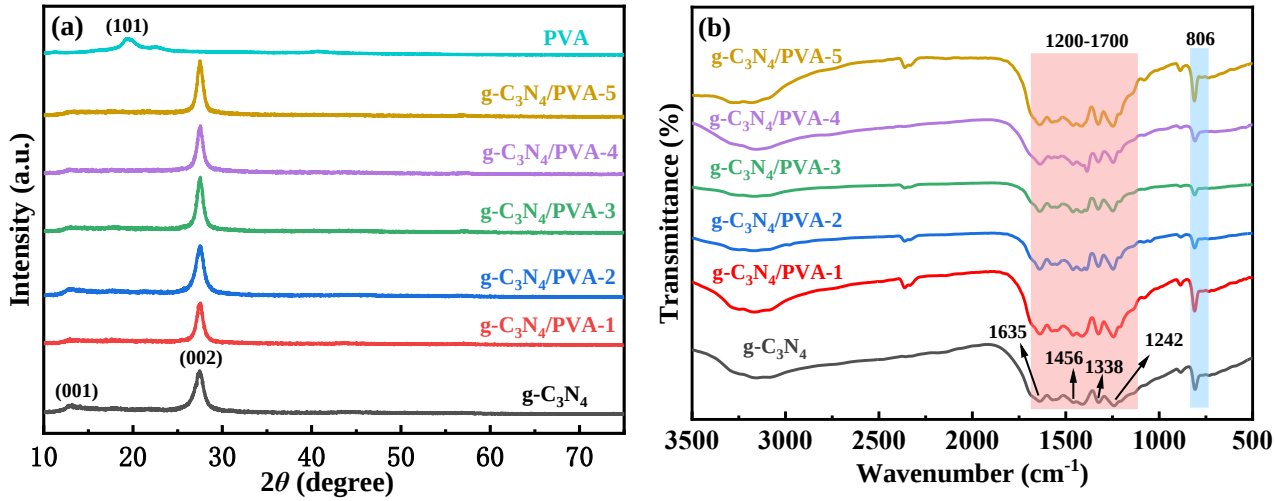

Figure 1. (a) XRD patterns, and (b) FT-IR spectra of g-C_3N_4 and g-C_3N_4/PVA heterojunction

approximately 6%. In contrast, the g-C_3N_4/PVA-3 composites exhibit significant weight loss (approximately 9%) within the temperature range of 300-400 ℃, suggesting that the composite material remains stable under the photocatalytic reaction conditions at temperatures below 100 ℃.

The N_2 adsorption-desorption isotherm curves were evaluated using the Brunauer-Emmett-Teller (BET) and Barrett-Joyner-Halenda models (BJH) methods. As shown in Figure 3(a), both g-C_3N_4 and g-C_3N_4/PVA-3 heterojunction display type IV isotherms with H3-type hysteresis loops, which suggest the presence of a mesoporous structure [34,35]. The BET specific surface areas of g-C_3N_4/PVA-3 and g-C_3N_4 were measured to be 12.79 and 29.35 m^2/g, respectively. Notably, the loading of PVA significantly increases the specific surface area, which is favorable for providing more active sites [34,35]. Additionally, the pore size distribution plots in Figure 3(b) further confirms that the pore sizes of g-C_3N_4 and g-C_3N_4/PVA-3 are mainly centered in the range of 2 nm to 20 nm, indicating that the obtained photocatalysts are mesoporous materials.

The UV-visible diffuse reflectance absorption spectrum (UV-vis DRS) is an excellent means for evaluating the light-harvesting capability of materials. As depicted in Figure 3(c), the UV-vis DRS of g-C_3N_4 and g-C_3N_4/PVA heterojunctions indicates that the latter demonstrates significantly enhanced absorption in the visible light region compared to pure g-C_3N_4. This enhanced absorption suggests improved visible-light photocatalytic performance for the g-C_3N_4/PVA heterojunctions. Moreover, the bandgap values (E_g) of the synthesized g-C_3N_4/PVA photocatalysts were estimated according to the Tauc plot method (Equation (4)) [36]. For g-C_3N_4, an indirect bandgap semiconductor [10], a plot of $(ahv)^{1/2}$ vs. (hv) [10], and the linear part in Figure 3(d) is extended to y

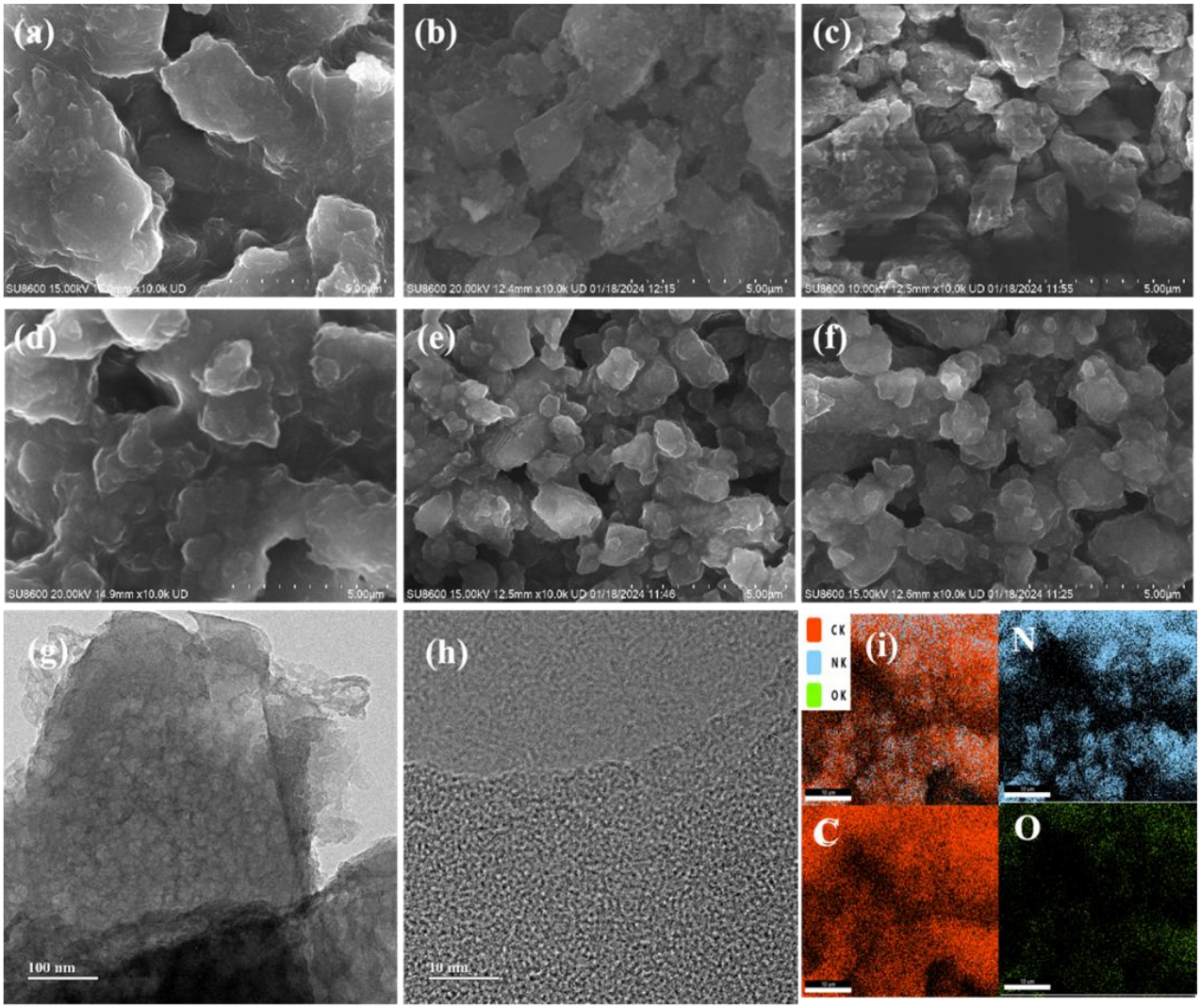

Figure 2. SEM images of (a) g-C_3N_4, (b) g-C_3N_4/PVA-1, (c) g-C_3N_4/PVA-2, (d) g-C_3N_4/PVA-3, (e) g-C_3N_4/PVA-4, (f) g-C_3N_4/PVA-5, and (g) EDX spectrum and elemental mapping images of g-C_3N_4/PVA-3, (h)HRTEM of g-C_3N_4/PVA-3, and (i) elemental mapping images of g-C_3N_4/PVA-3.

= 0, yielding the bandgap values for g-C_3N_4 and g-C_3N_4/PVA. The results show that the E_g of g-C_3N_4 is 2.66 eV, while those for g-C_3N_4/PVA-1, g-C_3N_4/PVA-2, g-C_3N_4/PVA-3, g-C_3N_4/PVA-4 and g-C_3N_4/PVA-5 are 2.66, 2.69, 2.73, 2.73, 2.73 and 2.75 eV, respectively. Where α, h, υ, E_g, and A denote the absorption coefficient, Planck's constant, light frequency, band gap, and proportionality constant, respectively.

$$\alpha h\upsilon = A\left(h\upsilon - E_g\right)^{1/2} \quad (4)$$

3.2. Photocatalytic Performance Evaluation

The photocatalytic performance of the prepared g-C_3N_4 and g-C_3N_4/PVA heterojunctions was assessed through the photocatalytic reduction of aqueous Cr(VI). At least three parallel photocatalytic experiments were conducted under each condition to ensure the experimental error was maintained within 5%. The relevant experimental results are presented in the form of error bars in Figure 4(a) and (c). Additionally, the rates of the photocatalytic reduction reaction were analyzed using a pseudo-first-order kinetic model (Equation (5)):

$$\ln\left(\frac{c_{i0}}{c_{it}}\right) = kt \quad (5)$$

Here, c_{it} and c_{i0} denote the concentration of aqueous Cr(VI) at time t and the initial moment (0 min) under light irradiation, respectively. As illustrated in Figure 4(b), the rate constants for the photocatalytic reduction of Cr(VI) using various photocatalysts were determined from the plot of $\ln(c_{i0}/c_{it})$ versus time. As shown in Figure 4(a) and Figure 4(b), pure g-C_3N_4 achieved a photocatalytic reduction rate of 38.2% for Cr(VI) after 120 min of exposure to visible light, with a corresponding reaction rate constant of approximately 0.0058 min^{-1}. In contrast, the g-C_3N_4/PVA heterojunction all exhibited enhanced photocatalytic activities, with g-C_3N_4/PVA-3 showing the highest activity, achieving a photocatalytic reduction rate of 80.2%, which is 2.93 times that of pure g-C_3N_4. Additionally, it was found that the introduction of 0.5 mol/L formic acid solution as a hole scavenger in the reaction system significantly improved the photocatalytic efficiency.

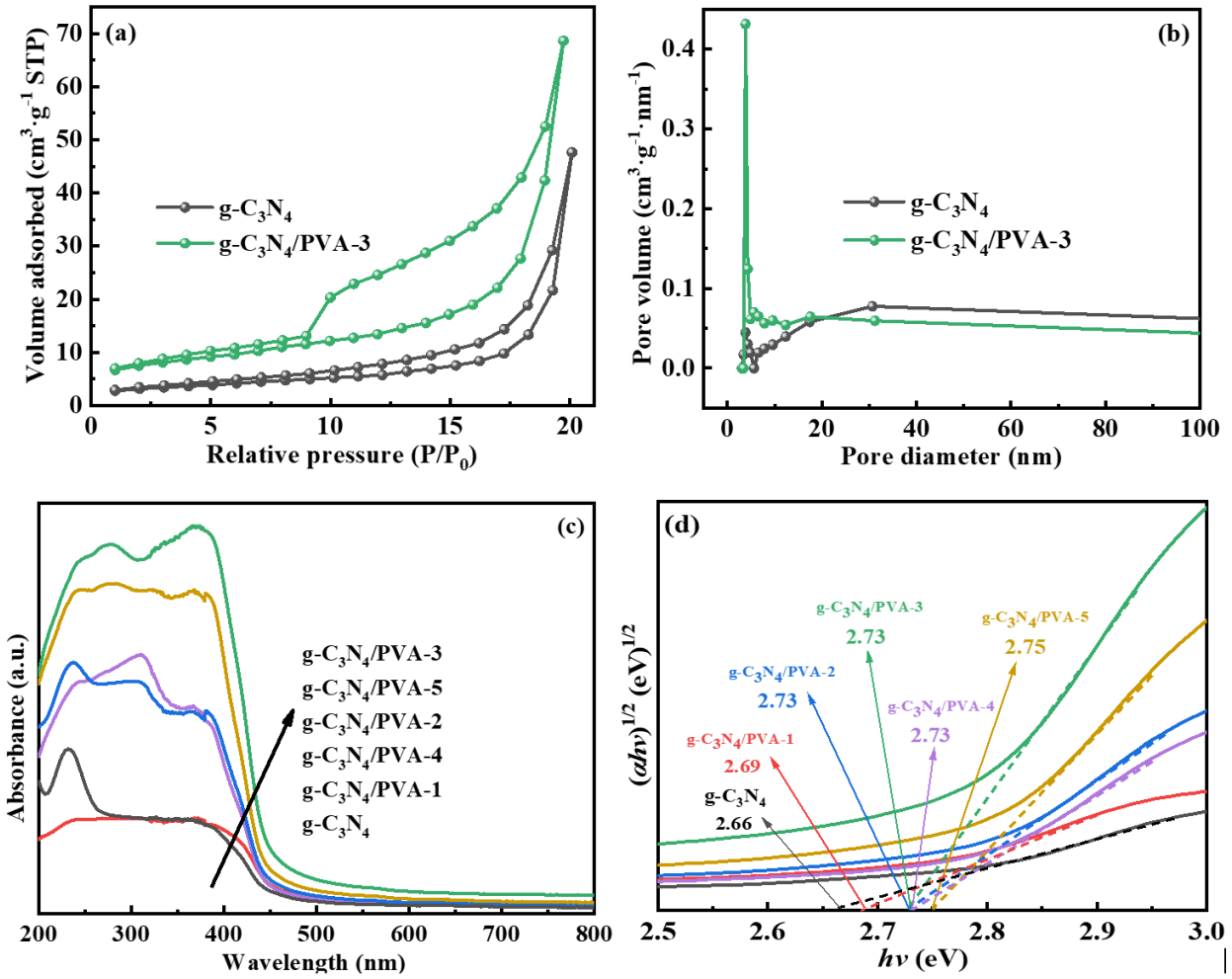

Figure 3. (a) N_2 adsorption-desorption isotherms, (b) pore size distribution curves, (c) UV-vis DRS spectra, and (d) bandgap values of the g-C_3N_4 and g-C_3N_4/PVA heterojunction.

As depicted in Figure S4(a) (Supporting Information), the photocatalytic reduction efficiency of g-C_3N_4/PVA-3 for Cr(VI) was investigated with varying catalyst dosages ranging from 200 mg to 500 mg. The Cr(VI) reduction rate gradually increased as the catalyst dosage was augmented. Notably, the reduction rate improved progressively when the catalyst dosage reached 500 mg. This observation indicates that increasing the catalyst dosage can effectively enhance reaction efficiency. Figure S4(b) (Supporting Information) presents the photocatalytic reduction efficiency of g-C_3N_4/PVA-3 and g-C_3N_4 for Cr(VI) under different temperature conditions. The experimental findings reveal that Cr(VI) reduction rate by both g-C_3N_4/PVA-3 and g-C_3N_4 increases with rising temperature. Based on the Arrhenius equation, the activation energies for Cr(VI) reduction by g-C_3N_4/PVA-3 and g-C_3N_4 were calculated to be 53 kJ/mol and 87 kJ/mol, respectively. These results demonstrate that PVA modification significantly reduces the reaction energy barrier, enhancing the photocatalytic reduction efficiency of Cr(VI). Figure 4(c) showed that the addition of 1.0 mL of formic acid solution almost eliminated Cr(VI) in water after 120 min of illumination. To reveal the active species in the photocatalytic reduction of Cr(VI) by g-C_3N_4/PVA, isopropanol (IPA) and benzoquinone (BQ) were introduced as molecular quenchers for hydroxyl radicals (•OH) and superoxide radicals ($•O_2^-$), respectively. Figure 4(d) revealed that the presence of IPA and BQ inhibited the reduction rate of Cr(VI) to 53.2% and 37.7%, respectively, indicating that both •OH and $•O_2^-$ radicals played important roles in the photocatalytic reduction of Cr(VI). Therefore, it can be inferred that h^+, •OH, and $•O_2^-$ act as active radicals in the photocatalytic reaction.

Furthermore, it was observed that introducing a 0.5 mol/L formic acid solution as a hole scavenger in the reaction system significantly enhanced the photocatalytic efficiency. As illustrated in Figure 4(c), adding 1.0 mL of formic acid solution nearly eliminated Cr(VI) from the water after 120 minutes of illumination. To identify the active species involved in the photocatalytic reduction of Cr(VI) by g-C_3N_4/PVA, isopropanol (IPA) and benzoquinone (BQ) were employed as quenchers for hydroxyl radicals (•OH) and superoxide radicals ($•O_2^-$), respectively. Figure 4(d) shows that the presence of IPA and BQ reduced the Cr(VI) reduction rate to 53.2% and 37.7%, respectively, indicating that both •OH and $•O_2^-$ radicals play crucial roles in the photocatalytic reduction process. Consequently, it can be concluded that h^+, •OH, and $•O_2^-$ serve as the primary active species in the photocatalytic reaction. The stability of g-C_3N_4/PVA, which exhibits the highest photocatalytic activity, was evaluated, and the results are presented in Figure 4(e). The g-C_3N_4/PVA-3 can still remove approximately 77.8% of Cr(VI) from an aqueous solution after five cycles of photocatalytic experiments. This value is only slightly lower than the initial Cr(VI) removal rate

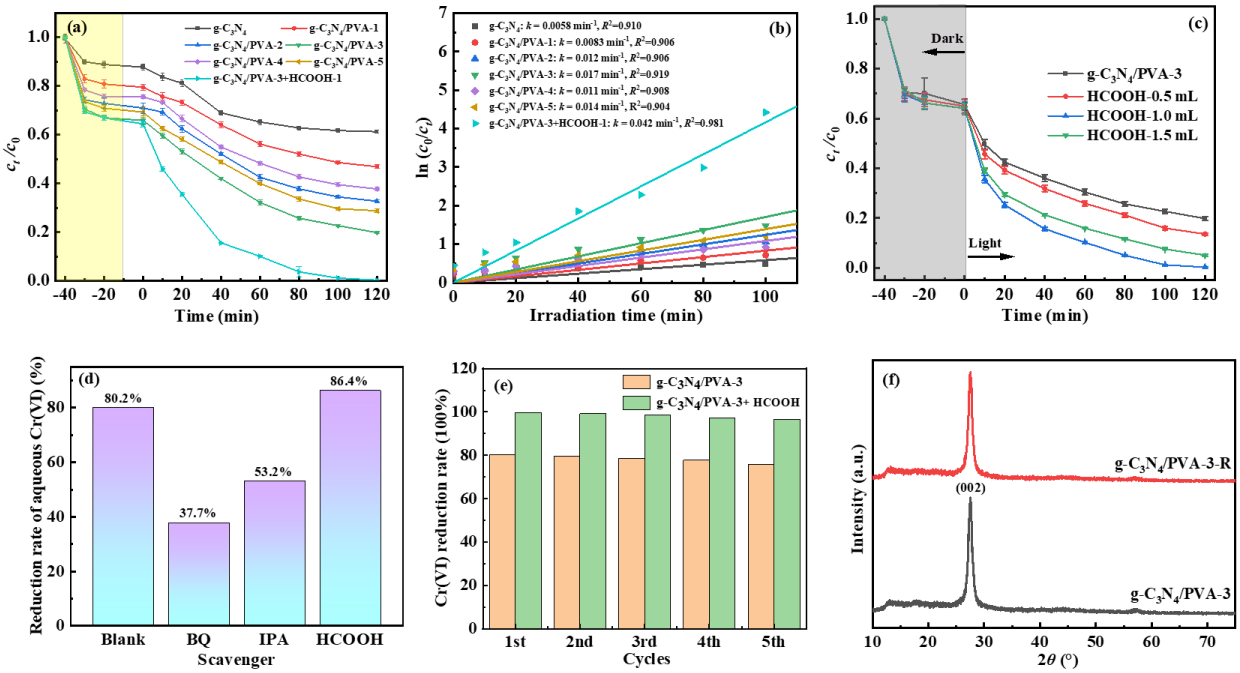

Figure 4. (a) Comparison of photocatalytic activities, (b) the reaction rate constants (k) for the photocatalytic reduction of Cr(VI) derived from ln (c_{i0}/c_{it}) vs. ti plots, (c) Influence of formic acid dosageas as a trapping agent on the efficiency of Cr(VI) reduction, and (d) radical scavenging experiments during the Cr(VI) reduction by g-C_3N_4 and g-C_3N_4/PVA heterojunctions. (e) The photocatalytic stability of g-C_3N_4/PVA-3, (f) XRD patterns of g-C_3N_4/PVA-3 heterojunction before and after photocatalysis.

of 80.2%, demonstrating that g-C_3N_4/PVA possesses outstanding photocatalytic stability. The XRD patterns of g-C_3N_4/PVA-3 after the photocatalytic reaction, as depicted in Figure 4(f), have hardly changed compared to the freshly synthesized g-C_3N_4/PVA-3. This observation indicates that the crystalline phase of g-C_3N_4/PVA-3 is preserved throughout the photocatalytic experiment.

We prepared three independent batches of g-C_3N_4/PVA-3 and evaluated their performance in the photocatalytic reduction of Cr(VI) to ensure the reproducibility of the experimental results. As depicted in Figure S5 (Supporting Information), the deviation in the experimental results was less than 5%, which substantiates the reliability of the synthetic protocol. To further assess the photocatalytic efficiency, we calculated the Turn Over Frequency (TOF) for the g-C_3N_4/PVA-3-mediated photocatalytic reduction of Cr(VI), yielding a value of 0.0079 h^{-1}. This figure is comparable to the reported TOF values of 0.0081 h^{-1} for U(VI) reduction by $ZnFe_2O_4$/g-C_3N_4 [9] and 0.0082 h^{-1} for Cr(VI) reduction by CPVA/$ZnFe_2O_4$ [31]. These findings indicate that g-C_3N_4/PVA-3 is an effective photocatalyst.

3.3 Mechanism of Enhanced Photocatalytic Activity of g-C_3N_4/PVA

To elucidate the enhanced photocatalytic performance of g-C_3N_4/PVA, electrochemical impedance spectroscopy (EIS), transient photocurrent response (TPC), and photoluminescence (PL) measurements were employed to assess the migration behavior and separation efficiency of photogenerated charge carriers in the semiconductor. The Nyquist plots indicated that a smaller semicircle diameter correlates with reduced carrier transfer resistance in the sample. As shown in Figure 5(a), the Nyquist plots indicate that the charge transfer resistance of all g-C_3N_4/PVA heterojunctions is less than that of pure g-C_3N_4, with the g-C_3N_4/PVA-3 exhibiting the lowest charge transfer resistance. The transient photocurrent results in Figure 5(b) show that g-C_3N_4/PVA-3 has the highest photocurrent density, approximately 3.5 times that of pure g-C_3N_4, confirming its fastest photogenerated carrier separation efficiency.

Research has demonstrated that a relatively weak photoluminescence (PL) peak generally signifies a reduced recombination rate of h^+ and e^- in semiconductor photocatalysts [14,18]. As shown in Figure S6 (Supporting Information), the PL emission spectra indicate that the PL peak intensities for g-C_3N_4/PVA heterojunctions are uniformly lower than those of pure g-C_3N_4. Specifically, the g-C_3N_4/PVA-3 sample displays the lowest PL peak intensity, implying that the recombination of photogenerated charge carriers is markedly suppressed in this composite material. This finding further corroborates that the g-C_3N_4/PVA heterojunction improves the separation efficiency of charge carriers, effectively minimizing the direct recombination of h^+ and e^-, thus enhancing photocatalytic performance.

The band structure of the g-C_3N_4 and g-C_3N_4/PVA heterojunctions were evaluated according to their Mott-Schottky plots. The Mott-Schottky plots in Figure 6, which are positively sloped for both g-C_3N_4 and g-C_3N_4/PVA-3, suggesting that they are n-type semiconductors [37], and the loading of PVA did not alter the semiconductor type of g-C_3N_4. According to the extrapolation method where $1/C^2 = 0$, the flat band potentials (E_{FB}) of g-C_3N_4 and g-C_3N_4/PVA-3 (*vs.* Ag/AgCl) were determined to be −0.60 and −0.79 eV, respectively. According to the conversion E_{FB} (vs. NHE) = E_{FB} (vs. SCE) + 0.222 + 0.0592 × pH [38], with the potential of the reference electrode AgCl/Ag is 0.222 V, and knowing that the E_{CB} (vs. NHE) for n-type semiconductors is

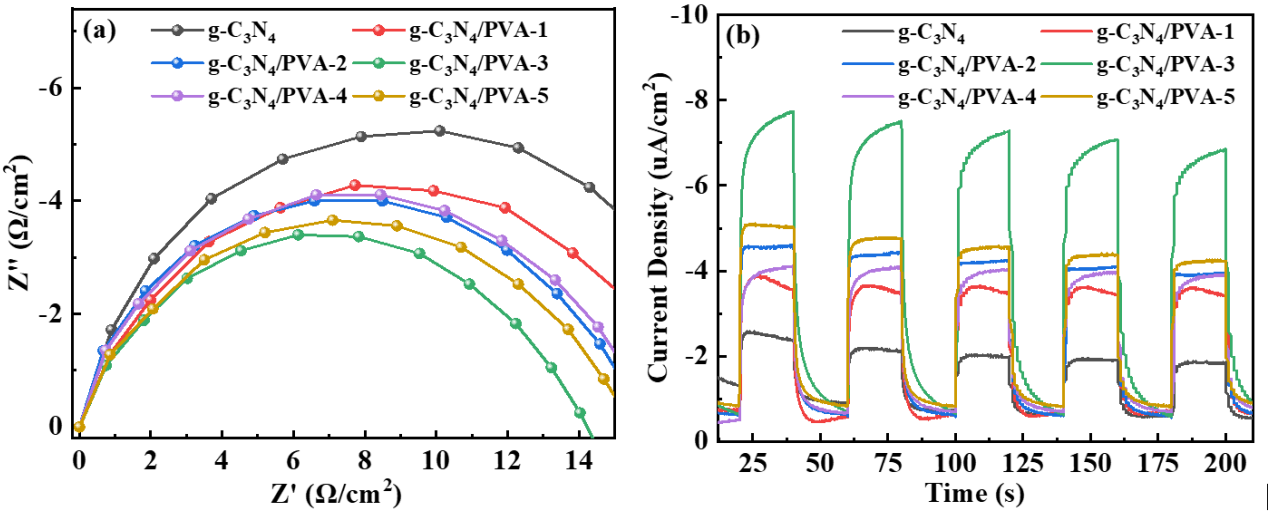

Figure 5. (a) Electrochemical impedance spectra, (b) Transient photocurrent response of g-C_3N_4 and g-C_3N_4/PVA heterojunction.

0.10 to 0.30 eV lower than E_{FB} (vs. NHE) (this article takes 0.3). The E_{CB} (vs. NHE) for g-C_3N_4 and g-C_3N_4/PVA-3 were calculated to be −0.264 eV and −0.454 eV, respectively. Furthermore, according to $E_{VB} = E_g + E_{CB}$, the E_{CB} (vs. NHE) for g-C_3N_4 and g-C_3N_4/PVA-3 were determined to be +2.396 and +2.276 eV, respectively.

According to the literature, the highest occupied molecular orbital (HOMO) and the lowest unoccupied molecular orbital (LUMO) of polyvinyl alcohol (PVA) are reported to be 1.9 eV and −0.5 eV, respectively [25]. In a conventional type II g-C_3N_4/PVA heterojunction, photogenerated electrons tend to accumulate in the conduction band of g-C_3N_4, while photogenerated holes localize in the valence band of PVA at 1.9 eV. Given that the conduction band edge of g-C_3N_4 (−0.264 eV) is less negative than the reduction potential of $O_2/\cdot O_2^-$ (−0.33 eV), and the LUMO energy level of PVA (1.9 eV) exceeds the oxidation potentials of $\cdot OH/H_2O$ (2.37 eV) and Cr(VI)/Cr(III) (1.99 eV), it would suggest that the effective generation of $\cdot O_2^-$ and ·OH radicals within this type II heterojunction should not be feasible. However, this theoretical prediction contradicts the experimental findings from the radical trapping experiments.

Based on the band structure and the analysis of active species, an S-scheme photocatalytic mechanism for the g-C_3N_4/PVA heterojunction in the reduction of Cr(VI) is proposed, as shown in Figure 7. At the closely integrated heterointerface between g-C_3N_4 and PVA, photogenerated electrons from g-C_3N_4 and holes from PVA recombine at the interface. This process reduces bulk recombination within the individual components and retains photogenerated electrons with strong reducing capabilities in the LUMO of PVA and holes with strong oxidizing capabilities in the valence band of g-C_3N_4. Unlike conventional type II heterojunctions, such as BiOI/g-C_3N_4 [7], the S-scheme charge transfer mechanism in g-C_3N_4/PVA sustains a high REDOX potential by efficiently recombining inactive carriers at the interface. This process significantly enhances the generation of $\cdot O_2^-$ and ·OH (Figure 4d), directly increasing the TOF of the target reaction.

4. Conclusion

In summary, a novel S-scheme g-C_3N_4/PVA heterojunction was successfully fabricated via in-situ hydrothermal modification combined with hot-quenched bonding. Among the prepared samples, g-C_3N_4/PVA-3 exhibited a markedly enhanced visible-light-driven photocatalytic reduction rate for Cr(VI), achieving a rate constant of 0.017 min^{-1}, which is approximately 2.93 times higher than that of pristine g-C_3N_4, with a TOF value of 0.0079 h^{-1}. Structural characterization and photoelectrochemical analysis revealed that the synergistic effects of nitrogen vacancy defect suppression, extended visible light absorption, decreasing activation energy, and efficient S-scheme charge separation contributed to its superior performance. The primary active species identified were ·OH and $\cdot O_2^-$. Moreover, the g-C_3N_4/PVA composite retained 95% of its initial photocatalytic activity after five consecutive cycles, demonstrating excellent stability. This study not only proposes a cost-effective approach for designing high-performance photocatalysts but also elucidates the critical role of the polymer-semiconductor interface in regulating charge transfer processes.

Acknowledgement

This research was funded by Innovation and entrepreneurship projects for college students (xcx2024002).

CRediT Author Statement

Author Contributions: Tianhong Guo: Design, Writing - Review & Editing. Yingxing Jiang and Yuanyuan Luo: Investigation & Funding, Visualization. Xinshan Zhao: Investigation. Jing

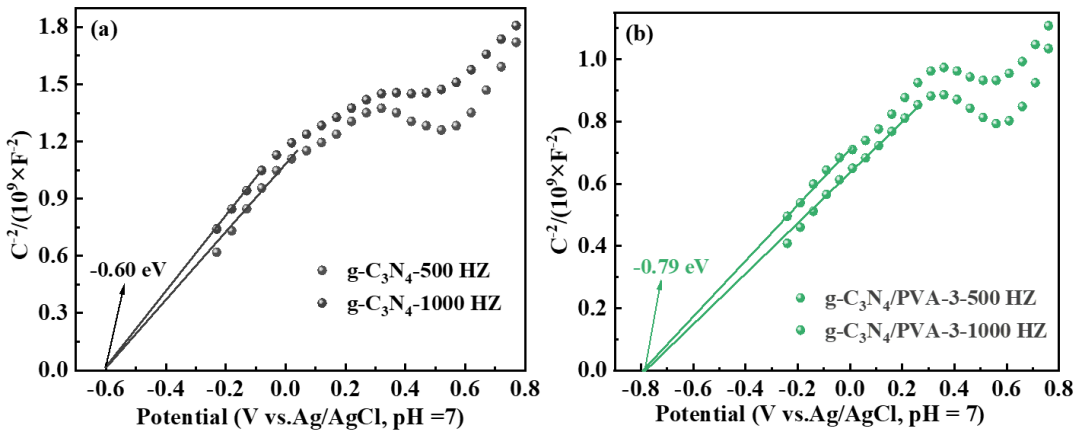

Figure 6. Mott-Schottky plots of the g-C_3N_4 and g-C_3N_4/PVA-3 heterojunction.

Li: Review, Supervision & Formal analysis. All authors have read and approved the final version of the manuscript.

References

[1] Sun, Y., Szulejko, J. E., Kim, K. H., Kumar, V., Li, X. (2023). Recent advances in the development of bismuth-based materials for the photocatalytic reduction of hexavalent chromium in water. *Chinese Journal of Catalysis*, 55, 20-43. DOI: 10.1016/s1872-2067(23)64553-x.

[2] Hasija, V., Raizada, P., Singh, P., Verma, N., Khan, A. A. P., Singh, A., Selvasembian, R., Kim, S. Y., Hussain, C.M., Nguyen, V., Van Le, Q. (2021). Progress on the photocatalytic reduction of hexavalent Cr (VI) using engineered graphitic carbon nitride. *Process Safety and Environmental Protection*, 152, 663-678. DOI: 10.1016/j.psep.2021.06.042.

[3] Yan, W., Chen, Q., Meng, X., Wang, B. (2017). Multicycle photocatalytic reduction of Cr (VI) over transparent PVA/TiO_2 nanocomposite films under visible light. *Science China Materials*, 5(60), 449-460. DOI: 10.1007/s40843-017-9024-9.

[4] Zhao, X., Xu, M., Song, X., Zhou, W., Liu, X., Huo, P. (2022). 3D Fe-MOF embedded into 2D thin layer carbon nitride to construct 3D/2D S-scheme heterojunction for enhanced photoreduction of CO2. *Chinese Journal of Catalysis*, 43(10), 2625-2636. DOI: 10.1016/s1872-2067(22)64115-9.

[5] Balu, S., Chen, Y. L., Juang, R. C., Yang, T. C. K., Juan, J. C. (2020). Morphology-controlled synthesis of α–Fe_2O_3 nanocrystals impregnated on g-C_3N_4–SO_3H with ultrafast charge separation for photoreduction of Cr (VI) under visible light. *Environmental Pollution*, 267, 115491. DOI: 10.1016/j.envpol.2020.115491.

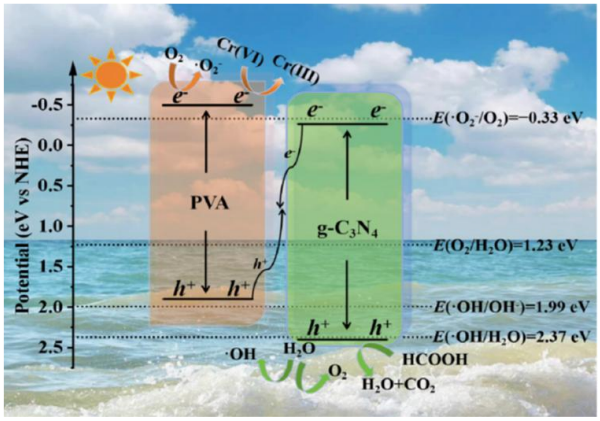

Figure 7. Mechanism for the photocatalytic reduction of Cr(VI) by g-C_3N_4/PVA-3 heterojunction.

[6] Dou, K., Peng, C., Wang, R., Cao, H., Yao, C., Qiu, J.,Liu, J., Tsidaeva, N., Wang, W. (2023). S-scheme tubular g-C_3N_4/BiOI heterojunctions for boosting photodegradation of tetracycline and Cr (VI): Mechanism insight, degradation pathway and DFT calculation. *Chemical Engineering Journal*, 455, 140813. DOI: 10.1016/j.cej.2022.140813.

[7] Zhang, H., Yang, J., Guo, L., Wang, R., Peng, S., Wang, J., Wang, W., Xu, J. (2021). Microwave-aided synthesis of BiOI/g-C_3N_4 composites and their enhanced catalytic activities for Cr (VI) removal. *Chemical Physics Letters*, 762, 138143. DOI: 10.1016/j.cplett.2020.138143.

[8] Uma, K., Pawar, S. (2023). TiO_2/g-C_3N_4 composites for the removal of chromium in wastewater. *Results in Chemistry*, 5, 100743. DOI: 10.1016/j.rechem.2022.100743.

[9] Dai, Z., Zhen, Y., Sun, Y., Li, L., Ding, D. (2021). $ZnFe_2O_4$/g-C_3N_4 S-scheme photocatalyst with enhanced adsorption and photocatalytic activity for uranium (VI) removal. *Chemical Engineering Journal*, 415, 129002. DOI: 10.1016/j.cej.2021.129002.

[10] Zhang, X., Zhao, Y., Li, J., Wang, Q., Yin, Y., Zhao, X. (2024). Enhanced photocatalytic activity in Pr^{3+}-doped Bi_2WO_6 through Nd^{3+} co-doping. *Functional Materials Letters*, 17(3), 2451013. DOI: 10.1142/s1793604724510135.

[11] Yu, Y., Chen, D., Xu, W., Fang, J., Sun, J., Liu, Z., Chen, Y., Liang, Y., Fang, Z. (2021). Synergistic adsorption-photocatalytic degradation of different antibiotics in seawater by a porous g-C_3N_4/calcined-LDH and its application in synthetic mariculture wastewater. *Journal of Hazardous Materials*, 416, 126183. DOI: 10.1016/j.jhazmat.2021.126183.

[12] Ma, B., Zha, Y., Yu, P., Chen, G., Guo, Y., Lan, Y., Li, J., Xia, W., Zhao, B. (2023). Hydrothermal nanoarchitectonics of Z-scheme g-C_3N_4/Bi_2WO_6 heterojunction with enhanced adsorption and photocatalytic activity for fluoroquinolone antibiotics removal: kinetics, mechanism and degradation pathway. *Journal of Alloys and Compounds*, 952, 170061. DOI: 10.1016/j.jallcom.2023.170061. .

[13] Wang, L., Yang, T., Peng, L., Zhang, Q., She, X., Tang, H., Liu, Q. (2022). Dual transfer channels of photo-carriers in 2D/2D/2D sandwich-like $ZnIn_2S_4$/g-C_3N_4/Ti_3C_2 MXene S-scheme/Schottky heterojunction for boosting photocatalytic H2 evolution. *Chinese Journal of Catalysis*, 43(10), 2720-2731. DOI: 10.1016/s1872-2067(22)64133-0.

[14] Fang, J., Xie, K., Kang, Q., Gou, Y. (2022). Facile fabrication of g-C_3N_4/CdS heterojunctions with enhanced visible-light photocatalytic degradation performances. *Journal of Science: Advanced Materials and Devices*, 7(1), 100409. DOI: 10.1016/j.jsamd.2021.100409.

[15] Ma, Y., Jia, Y. L., Lin, Y. H., Shi, W. B. (2021). Hierarchical Brookite TiO_2–Bi_2MoO_6 Nanospheres with Efficient Visible-Light-Driven Photocatalytic Response. *Journal of Nanoscience and Nanotechnology*, 21(10), 5370-5377. DOI: 10.1166/jnn.2021.19344.

[16] Yi, F., Ma, J., Lin, C., Wang, L., Zhang, H., Qian, Y., Zhang, K. (2020). Insights into the enhanced adsorption/photocatalysis mechanism of a $Bi_4O_5Br_2$/g-C_3N_4 nanosheet. *Journal of Alloys and Compounds*, 821, 153557. DOI: 10.1016/j.jallcom.2019.153557.

[17] Liu, C., Dai, H., Tan, C., Pan, Q., Hu, F., Peng, X. (2022). Photo-Fenton degradation of tetracycline over Z-scheme Fe-g-C_3N_4/Bi_2WO_6 heterojunctions: Mechanism insight, degradation pathways and DFT calculation. *Applied Catalysis B: Environmental*, 310, 121326. DOI: 10.1016/j.apcatb.2022.121326.

[18] Yin, Z., Tian, Y., Gao, P., Feng, L., Liu, Y., Du, Z., Zhang, L. (2020). Photodegradation mechanism and genetic toxicity of bezafibrate by Pd/g-C_3N_4 catalysts under simulated solar light irradiation: The role of active species. *Chemical Engineering Journal*, 379, 122294. DOI: 10.1016/j.cej.2019.122294.

[19] Liu, Y., Yin, W., Lin, Q., Li, Z., Zhong, W., Fang, B. (2023). Nitrogen vacancies-engineered graphitic carbon nitride nanosheets for boosting photocatalytic H_2 production. *Applied Surface Science*, 640, 158386. DOI: 10.1016/j.apsusc.2023.158386.

[20] Li, J., Li, K., Du, J., Yang, H., Song, C., Guo, X. (2022). Impact of transition metal incorporation on the photocatalytic CO_2 reduction activity of polymeric carbon nitride. *Journal of CO2 Utilization*, 64, 102162. DOI: 10.1016/j.jcou.2022.102162.

[21] Praus, P. (2023). Photocatalytic nitrogen fixation using graphitic carbon nitride: A review. *ChemistrySelect*, 8(1), e202204511. DOI: 10.1002/slct.202204511.

[22] Mazzanti, S., Markushyna, Y., Savateev, O. (2023). Photocatalytic C− H Amination of Electron-rich Aromatic Hydrocarbons by Carbon Nitride Photocatalysis. *ChemCatChem*, 15(5), e202201388. DOI: 10.1002/cctc.202201388.

[23] Zuo, M., Li, X., Liang, Y., Zhao, F., Sun, H., Liu, C., Gong, X., Qin, P., Wang, H., Wu, Z., Luo, L. (2023). Modification of sulfur doped carbon nitride and its application in photocatalysis. *Separation and Purification Technology*, 308, 122875. DOI: 10.1016/j.seppur.2022.122875.

[24] Zhang, Q., Liu, S., Zhang, Y., Zhu, A., Li, J., Du, X. (2016). Enhancement of the photocatalytic activity of g-C_3N_4 via treatment in dilute NaOH aqueous solution. *Materials Letters*, 171, 79-82. DOI: 10.1016/j.matlet.2016.02.043.

[25] Sun, M., Wang, Y., Huang, A., Tian, Y., Yang, R., Wang, H., Zhao, X., Song, X. (2023). Naturally flavonoid-derived PVA nanofibers for antioxidation. *New Journal of Chemistry*, 47(29), 14046-14055. DOI: 10.1039/d3nj01990j.

[26] Liu, S., Gao, X., Fan, H., Zhang, M., Waterhouse, G. I., Zhu, S. (2023). Green and recyclable graphitic carbon nitride/chitosan/polyvinyl alcohol photocatalytic films with efficient antibacterial activity for fruit packaging. *International Journal of Biological Macromolecules*, 236, 123974. DOI: 10.1016/j.ijbiomac.2023.123974.

[27] Wang, K., Chen, P., Nie, W., Xu, Y., Zhou, Y. (2019). Improved photocatalytic reduction of Cr (VI) by molybdenum disulfide modified with conjugated polyvinyl alcohol. *Chemical Engineering Journal*, 359, 1205-1214. DOI: 10.1016/j.cej.2018.11.057.

[28] Gao, X., Ai, L., Wang, L., Ju, Y., Liu, S., Wang, J., Fan, H. (2022). The stable and elastic graphitic carbon nitride/polyvinyl alcohol photocatalytic composite sponge: Simple synthesis and application for wastewater treatment. *Journal of Environmental Chemical Engineering*, 10(3), 107814. DOI: 10.1016/j.jece.2022.107814.

[29] Chen, C., Liao, F., Zhang, X., Cheng, S., Deng, Y., Chen, C., Long, M. (2024). Polyvinyl alcohol as solid proton donor to modify g-C_3N_4 via hydrogen bonding enabling efficient photocatalytic H_2O_2 production from H_2O and O_2. *RSC Advances*, 14(18), 12407-12415. DOI: 10.1039/d4ra01746c.

[30] Adorna Jr, J., Annadurai, T., Bui, T. A. N., Tran, H. L., Lin, L. Y., Doong, R. A. (2021). Indirect Z-scheme nitrogen-doped carbon dot decorated Bi_2MoO_6/g-C_3N_4 photocatalyst for enhanced visible-light-driven degradation of ciprofloxacin. *Chemical Engineering Journal*, 422, 130103. DOI: 10.1016/j.cej.2021.130103.

[31] Du, Z., Liu, F., Ding, G., Dan, Y., Jiang, L. (2021). Effective degradation of tetracycline via polyvinyl alcohol/Bi_2WO_6 hybrid hydrogel with easy separation. *Materials Chemistry and Physics*, 262, 124239. DOI: 10.1016/j.matchemphys.2021.124239.

[32] Kumar, V. D., Kumari, S., Balaji, K. R., Khan, A. A., Ravikumar, C. R., Basavaraja, B. M.,Santosh, M. S., Rtimi, S. (2023). Singlet oxygen driven enhanced photocatalytic degradation of 1, 3, 7-trimethylpurine-2, 6-dione using surfactant mediated PVA-CuO nanocomposites: Combining physical adsorption and photocatalysis. *Chemical Engineering Journal*, 462, 142187. DOI: 10.1016/j.cej.2023.142187.

[33] Hosseini, S. F., Dorraji, M. S. S., Rasoulifard, M. H. (2023). Boosting photo-charge transfer in 3D/2D TiO_2@ Ti_3C_2 MXene/Bi_2S_3 Schottky/Z-scheme heterojunction for photocatalytic antibiotic degradation and H_2 evolution. *Composites Part B: Engineering*, 262, 110820. DOI: 10.1016/j.compositesb.2023.110820.

[34] Hosseini, A., Faghihian, H., Sanati, A. M. (2018). Elimination of dibenzothiophene from transportation fuel by combined photocatalytic and adsorptive method. *Materials Science in Semiconductor Processing*, 87, 110-118. DOI: 10.1016/j.mssp.2018.07.017.

[35] Jamaluddin, N. S., Alias, N. H., Samitsu, S., Othman, N. H., Jaafar, J., Marpani, F., Lau, W. J., Tan, Y. Z. (2022). Efficient chromium (VI) removal from wastewater by adsorption-assisted photocatalysis using MXene. *Journal of Environmental Chemical Engineering*, 10(6), 108665. DOI: 10.1016/j.jece.2022.108665.

[36] Hashem, E. M., Hamza, M. A., El-Shazly, A. N., Abd El-Rahman, S. A., El-Tanany, E. M., Mohamed, R. T., Allam, N. K. (2021). Novel Z-Scheme/Type-II CdS@ ZnO/g-C_3N_4 ternary nanocomposites for the durable photodegradation of organics: Kinetic and mechanistic insights. *Chemosphere*, 277, 128730. DOI: 10.1016/j.chemosphere.2020.128730.

[37] Bai, Y., Mao, W., Wu, Y., Gao, Y., Wang, T., Liu, S. (2021). Synthesis of novel ternary heterojunctions via Bi2WO6 coupling with CuS and g-C_3N_4 for the highly efficient visible-light photodegradation of ciprofloxacin in wastewater. *Colloids and Surfaces A: Physicochemical and Engineering Aspects*, 610, 125481. DOI: 10.1016/j.colsurfa.2020.125481.

[38] Paramanik, L., Subudhi, S., Parida, K. M. (2022). Visible light active titanate perovskites: An overview on its synthesis, characterization and photocatalytic applications. *Materials Research Bulletin*, 155, 111965. DOI: 10.1016/j.materresbull.2022.111965.